Parameter-fitting-free Continuum Modeling of Electric Double Layer in Aqueous Electrolyte

Masao Suzuki Shibata [a,b,*] , *Yu Morimoto* [a], *Iryna V. Zenyuk* [a], *Adam Z. Weber* [b]

a: Department of Chemical and Biomolecular Engineering; National Fuel Cell Research Center, University of California, Irvine, Irvine, CA 92697.

b: Energy Conversion Group, Lawrence Berkeley National Laboratory, 1 Cyclotron Rd, Berkeley, CA 94720.

*: masaos@lbl.gov

KEYWORDS

Electric Double Layer, Multiscale Continuum Modeling, Grand Potential,

ABSTRACT

Electric double layers (EDLs) play fundamental roles in various electrochemical processes. Despite the extensive history of EDL modeling, there remain challenges in accurate prediction of its structure without expensive computation. Herein, we propose a predictive multiscale continuum model of EDL that eliminates the need for parameter fitting. This model computes the distribution of the electrostatic potential, electron density, and species' concentrations by taking the extremum of the total grand potential of the system. The grand potential includes the microscopic interactions that are newly introduced in this work: polarization of solvation shells, electrostatic interaction in parallel plane toward the electrode, and ion-size-dependent entropy. The parameters that identify the electrode and electrolyte materials are obtained from independent experiments in the literature. The model reproduces the trends in the experimental differential capacitance with multiple electrode and nonadsorbing electrolyte materials (Ag (110) in NaF, Ag (110) in $NaClO_4$, and Hg in NaF), which verifies the accuracy and predictiveness of the model, and rationalizes the observed values to be due to changes in electron stability. However, our calculation on Pt (111) in $KClO_4$ suggests the need for incorporation of electrode/ion specific interactions. Sensitivity analyses confirmed that effective ion radius, ion valence, the electrode's Wigner-Seitz radius, and the bulk modulus of the electrode are significant material properties that control the EDL structure. Overall, the model framework and findings provide insights into EDL structures and predictive capability at low computational cost.

1. INTRODUCTION

The electric double layer (EDL) plays a fundamental role in various electrochemical processes such as colloidal dispersions, surface charging, and charge-transfer reactions. It appears at every electrode/electrolyte interface because of the work-function difference between the two materials. The work-function difference induces a strong electric field at the interface. The electric field redistributes the solute and solvent molecules in the electrolyte and forms a surface charge and dipole by either attracting or repulsing the molecules to or from the electrode surface. At the same time, electrons in the electrode also redistribute to form a surface charge and dipole by spilling into the electrolyte [1]. The surface charge due to the electron spillover is the same value in the opposite sign as that due to the redistribution of the molecules in the electrolyte, which ensures overall electroneutrality. The layered structure formed by the redistribution of electrons in the metal and molecules in the electrolyte is called the EDL.

The increasing focus of EDL studies lies on its impact on reaction kinetics. The electric-field strength and electrostatic potential near the interface is determined by the EDL structure, which can impact the concentration and stability of the reactants. Ringe et al [2] and Shin et al. [3] suggested that the electric-field strength at the interface can impact the stability of CO_2 adsorbent and thus the reaction kinetics of CO_2 reduction. Similar effects of EDLs on reaction kinetics can appear in any catalytic reactions in electrochemical systems. A deeper understanding of these effects will provide guidance for tailoring electrode/electrolyte interface with improved reaction kinetics.

Differential capacitance (C_d) has been analyzed as a fundamental property of EDLs [3-5]. C_d is defined as $C_d \equiv dQ/dV$, where Q is the surface charge density and V is the electrode potential. This property represents the potential dependence of the ion distribution in the electrolyte. C_d can be experimentally obtained by cyclic voltammetry (CV) or electrochemical-impedance

spectroscopy (EIS). In CV measurements, however, separating EDL capacitance from total capacitance can be challenging when a Faradaic reaction occurs in the potential range of interest [6]. EIS measurements with appropriate analysis can separate those two currents based on the difference in their timescales [4].

As a continuum modeling approach, Gouy-Chapman-Stern (GCS) theory has been widely used as a standard model for analyzing the EDL structures [1,5, 7-10]. This model envisions the EDL as two separate layers: Stern layer and diffuse layer. The Stern layer is a layer between the electrode surface and the closest approach of hydrated ions. In this layer, hydrated ions cannot exist because of size exclusion. Without specific ion adsorption, the Stern layer does not contain charged species. The dielectric constant in Stern layer can be much smaller than that of the bulk solvent (~ an order of magnitude) due to impacts of water structure [11-15] and field effects [16-18] near the interface. Unlike in the Stern layer, ions can redistribute depending on the electrostatic potential in the diffuse layer. The distribution is obtained from the Poisson equation and the condition for thermodynamic equilibrium. The analytical solution for the ion distribution is called Gouy-Chapman distribution when the chemical potential of ions (μ_i) is described in the form of

$$\mu_i = k_B T \ln n_i/n_i^0 + z_i e_0 \phi, \quad (1)$$

where k_B is the Boltzmann constant, T is the temperature, n_i is the number density of solute i, n_i^0 is the number density of *i* in the bulk, z_i is the ionic valency, e_0 is the elementary charge, and ϕ is the electrostatic potential. Bikerman [19] improved the accuracy of the diffuse-layer model by modifying the entropy term (first term on right side) to account for the finite size of the ions. He obtained an analytical expression for the entropy term by assuming that all of the ions in the electrolyte have the same molar volume [20]. The continuum model based on GCS theory with

Bikerman modification is widely used as primitive EDL models because of its computational efficiency.

Conventional continuum models, however, are not capable of 'predicting' the EDL structure by themselves. They require parameter fitting especially for the parameters in the Stern layer. The shortcomings of the conventional continuum models stem from the fact that they do not explicitly account for several fundamental microscopic interactions near the interface [21] such as electron spillover and ion specific adsorption.

Quantum-mechanical calculations like density-functional theory (DFT) [22-24] provide the means for predictive analyses of the interface. DFT calculations capture the effect of electron spillover as well as the specific interactions between the electrode/solute, electrode/solvent, and solute/solvent. The analysis can be further improved by using *ab-initio* molecular-dynamics simulations (AIMDs) [25, 26]. AIMDs can include quantum mechanical interactions as well as steric restrictions and entropic contributions. However, because of their large computational cost to evaluate the average structure of the statistical equilibrium, these calculations are limited to a small volume that is typically not sufficient to capture a whole picture of the EDL structure accurately.

The advantages of continuum models and quantum-mechanical calculations can be achieved by coupling these two models. Joint density-functional theory (joint DFT) was proposed to combine the quantum DFTs and classical continuum model [27, 28]. Huang proposed a simple and effective model named density potential functional theory (DPFT) [20]. This model combines a classical continuum model based on GCS theory with Bikerman modification and a simplified quantum-mechanical calculation. For the quantum-mechanical model, he employed a jellium model with uniform electron-gas approximation [22]. A jellium model, which describes the positive charge

distribution in the electrode as a uniform background charge, is one of the simplest models that accounts for electron spillover into the electrolyte. Although the jellium model does not provide results with highest accuracy, it has been used for work-function analyses [29-33] and EDL modeling [34-36] due to its computational efficiency. The accuracy of a jellium model can be improved by using pseudopotentials [30-33]. Even with Huang's DPFT model [20], however, parameter fitting is needed to reproduce the experimental differential-capacitance measurements.

This study proposes a new modeling framework that gains the advantages of both continuum models and molecular-dynamics simulations, *i.e.*, accurate and predictive analyses with low computational cost. This model computes the distribution of the electrostatic potential, electron density, and species' concentrations by taking the extremum of the total grand potential of the system. The grand potential is calculated from entropic energy, electrostatic energy, electron energy, solute-solute interactions, and electrode/solute interactions. These energy expressions include not only the terms from previous papers [20], but also the microscopic interactions that are newly introduced in this work: polarization of solvation shells, electrostatic interaction in parallel plane toward the electrode, and ion-size-dependent entropy. All parameters that identify the electrode and electrolyte materials are obtained from independent experiments; in this way, the model is predictive and does not contain additional fitting parameters.

2. THEORY

2.1. General approach

The EDL is often assumed to be in a quasi-equilibrium [37] because of its rapid formation. The formation timescale can be roughly expressed as $10\ l_D^2/D$, where l_D is the Debye length and D is

the diffusion coefficient [38], and can scale from 10^{-9} to 10^{-6} s for 1 M to 1 mM of 1:1 electrolytes with diffusion coefficient of 10^{-9} m^2/s, which is much shorter than typical electrochemical measurements (*e. g.* EIS measurement with 100 kHz corresponds to time scale of 10^{-5} s). [1, 7]. Based on the timescale difference, it is reasonable to assume that EDL is in quasi-equilibrium. Also, we focus on potential windows in which Faradaic reaction rate is small so that the chemical potential gradient of solutes in EDL is negligible. Based on these assumptions, the distribution of electrostatic potential (ϕ), electron density (n_e), and species' number density (n_i) are obtained by taking the extremum of the total grand potential (Ω_{tot}) of the system [20, 37]. More specifically, n_e and n_i are obtained by minimizing Ω_{tot}, while ϕ is obtained by maximizing it [39]. Ω_{tot} can be expressed as a functional of these unknown variables (ϕ, n_e, and n_i) as

$$\Omega_{tot}[\phi(r), n_e(r), n_i(r)] \coloneqq \iiint \omega_{tot}(\phi(r), \nabla\phi(r), n_e(r), \nabla n_e(r), n_i(r), r)\, dr^3\,, \qquad (2)$$

where ω_{tot} is the local grand potential. Here, we assume the electrode is flat and ϕ, n_e, and n_i distribute uniformly in the plane parallel to the electrode. With this assumption, the grand potential can be simplified in 1-dimension to

$$\begin{aligned}\bar{\Omega}_{tot}[\phi(x), n_e(x), n_i(x)] &\coloneqq \frac{\Omega_{tot}}{V} \\ &= \frac{1}{L_{metal} + L_{sol}} \int_{-L_{metal}}^{L_{sol}} \omega_{tot}(\phi(x), \nabla\phi(x), n_e(x), \nabla n_e(x), n_i(x), x)\, dx\,, \end{aligned} \qquad (3)$$

where x describes the position in the direction perpendicular to the electrode. $x < 0$, $x = 0$, and $x > 0$ represent the electrode, electrode/electrolyte interface, and the electrolyte, respectively. V is the volume of the system. $x = -L_{metal}$ is the left end of the calculation domain that represents

the bulk metal, and $x = L_{sol}$ is the right end of the domain that represents the bulk solution. The local grand potential can be decomposed into 5 factors.

$$\omega_{tot}(\phi, \nabla\phi, n_e, \nabla n_e, n_i, x) = \omega_{mix}(n_i) + \omega_{els}(\phi, \nabla\phi, n_e, n_i, x) + \omega_{elec}(n_e, \nabla n_e, x) + \omega_{ss}(n_i) + \omega_{ws}(n_i, x), \quad (4)$$

where ω_{mix} is the mixing entropy, ω_{els} is the electrostatic energy, ω_{elec} is the electron energy, ω_{ss} is the solute-solute interaction, and ω_{ws} is the wall (electrode)-solute non-electrostatic interaction. The reference potentials of all the grand-potential components are based on the electrochemical potential in the bulk electrolyte (denoted by the superscript 0) so that the conditions to taking the extremum of $\bar{\Omega}_{tot}$, which is described in the next section, are satisfied in the bulk. The expressions for ω_{tot} are shown in Section 2.3 and tabulated in Table S1 – S3 in the Supporting Information (SI).

2.2. Variational analysis

$\phi(x)$, $n_e(x)$, and $n_i(x)$ are obtained from the condition to let $\bar{\Omega}_{tot}[\phi(x), n_e(x), n_i(x)]$ be the extremum. The condition can be written as $\delta\bar{\Omega}_{tot}/\delta\phi(x) = \delta\bar{\Omega}_{tot}/\delta n_e(x) = \delta\bar{\Omega}_{tot}/\delta n_i(x) = 0$ for any x. By considering that the local grand potential ω_{tot} depends not only on ϕ, n_e, and n_i, but on the first order gradient of ϕ and n_e ($\nabla\phi$ and ∇n_e), the conditions are expressed as

$$\frac{\partial\omega_{tot}}{\partial\phi} - \nabla\left(\frac{\partial\omega_{tot}}{\partial\nabla\phi}\right) = \frac{\partial\omega_{tot}}{\partial n_e} - \nabla\left(\frac{\partial\omega_{tot}}{\partial\nabla n_e}\right) = \frac{\partial\omega_{tot}}{\partial n_i} = 0, \quad (5)$$

where ϕ, n_e, and n_i need to satisfy these equations at any position of x. Eq. 5 provides the same number of equations as the number of unknown variables ($\phi(x)$, $n_e(x)$, and $n_i(x)$). Hence, the distributions of the variables are determined by numerically solving for these equations. For the

numerical calculations, we used COMSOL Multiphysics 6.1. One should note that the condition for ϕ corresponds to the Poisson equation, the condition for n_e corresponds to the electron-density model in jellium model, and the condition for n_i corresponds to the thermodynamic-equilibrium equation. The formula for the partial differential equations (PDEs) derived from Eq. 5 are shown in Section S3 in the SI.

2.3. Local grand potential expressions

2.3.1. Mixing entropy, ω_{mix}

Bikerman[19] proposed a model for the mixing entropy that accounts for the finite size of the species. This expression is frequently employed in continuum models for EDLs because of the availability of analytical solutions. However, the model is associated with the total free energy by assuming that all the species in the solution have the same molar volume [40-42], which is not always applicable to ions with different molecular size or hydration numbers.

There are several existing models that deal with the asymmetric size of solute molecules. For example, Gongadze and Iglic [43] proposed a model by modifying the Bikerman model, providing an analytical expression for solute concentrations with molecules size variation. Another model proposed by Maggs and Podgornik [44] accounted for the entropy due to the solvent. However, a comprehensive formulation of mixing entropy with asymmetric size effect has yet to be established. The Gongadze's model involves an unphysical segmentation of the solutes to achieve uniform size, while the Maggs' model solely accounts for solvent entropy, neglecting entropy loss of solutes due to the existence of other solutes.

Hence, we derived the mixing entropy (ω_{mix}) based on the partition function with a lattice model,

$$\omega_{mix}(n_i) = \varepsilon_{mix}^{id}(n_i) + \varepsilon_{mix}^{slv}(n_i) + \varepsilon_{mix}^{size}(n_i) - \sum_{i=1}^{N} n_i \mu_{mix,i}\,, \tag{6}$$

where ε_{mix}^{id} is the entropy from ideal mixing, ε_{mix}^{slv} is the solvent's entropy considering the finite size of the solute molecules, and ε_{mix}^{size} is the entropy due to the difference in the species' molar volume. $\mu_{mix,i}$ is the chemical potential due to the mixing in the bulk solution that is defined to make sure $\partial\omega_{mix}/\partial n_i = 0$ in the bulk. This mixing entropy is based on the partition function using a lattice model as

$$\varepsilon_{mix}^{id}(n_i) \coloneqq k_B T \sum_{i=1}^{N} n_i \ln n_i V_i\,, \tag{7}$$

$$\varepsilon_{mix}^{slv}(n_i) \coloneqq k_B T \frac{\eta_N}{V_N} \ln \eta_N\,, \tag{8}$$

$$\varepsilon_{mix}^{size}(n_i) \coloneqq k_B T \sum_{i=1}^{N-1} \left[\left(\frac{1}{V_i} - \frac{1}{V_{i+1}}\right) \eta_i \ln \eta_i\right], \tag{9}$$

$$\mu_{mix,i} \coloneqq \left.\frac{\partial\left(\varepsilon_{mix}^{id}(n_i) + \varepsilon_{mix}^{slv}(n_i) + \varepsilon_{mix}^{size}(n_i)\right)}{\partial n_i}\right|_{n_i = n_i^0}, \tag{10}$$

where N is the number of the solute species, V_i is the volume of one molecule of species i, $\eta_i \coloneqq 1 - \sum_{k \le i} n_k V_k$. Smaller i represents larger solute molecule so that $V_1 \ge V_2 \ge \cdots \ge V_N$. The derivation of these equations is shown in Section S2.1 in the SI. When all the solute molecules have the same molar volume this expression reduces to the conventional Bikerman model [19].

2.3.2. Electrostatic interactions, ω_{els}

The grand potential due to electrostatic interactions can be expressed by

$$\omega_{els}(\phi, \nabla\phi, n_e, n_i, x) = \omega_{els}^{ef}(\nabla\phi, x) + \omega_{els}^{chg}(\phi, n_e, n_i, x) + \omega_{els}^{pol}(\nabla\phi, n_i, x), \quad (11)$$

where ω_{els}^{ef} is the electric field energy, ω_{els}^{chg} is the Coulombic energy of charged species, and ω_{els}^{pol} is the polarization energy of solvent and solute molecules. In this study, ω_{els}^{ef} and ω_{els}^{chg} use conventional expressions based on the coulombic interactions [37].

$$\omega_{els}^{ef}(\nabla\phi, x) \coloneqq -\frac{1}{2}\epsilon_0\left(\epsilon_{op}^{m}\Theta(-x) + \epsilon_{op}^{s}\Theta(x)\right)|\nabla\phi|^2 \quad (12)$$

$$\omega_{els}^{chg}(\phi, n_e, n_i, x) \coloneqq e_0\phi\left(n_e^0\Theta(-x) - n_e + \sum_{i=1}^{N} z_i n_i\right) \quad (13)$$

where ϵ_0 is the vacuum permittivity, e_0 is the elementary charge, n_e^0 is the valent electron density in the bulk metal. $\Theta(x)$ is the Heaviside step function which takes a value of 1 when $x > 0$ and 0 when $x < 0$. $\Theta(x)$ is used to express the metal properties in $x < 0$ and solution properties in $x > 0$. ϵ_{op}^{m} and ϵ_{op}^{s} are the optical dielectric constant of the metal and solvent, respectively. ω_{els}^{pol} accounts for the dielectric saturation [16, 17] and the polarizability of hydrated ions [45, 46]. In the calculation, we assume that dielectric saturation of ion solvation shell takes place in a similar way to water molecules [17, 46]:

$$\omega_{els}^{pol}(\nabla\phi, n_i, x) \coloneqq -\frac{3\epsilon_0\left(\epsilon_{eff}^{\nabla\phi=0}(n_i) - \epsilon_{op}^{s}\right)}{a_{pol}^2}\Theta(x)\ln\left(\frac{\sinh\left(a_{pol}\nabla\phi\right)}{a_{pol}\nabla\phi}\right), \quad (14)$$

where a_{pol} is a constant that controls the significance of dielectric saturation: large a_{pol} increase the effect of electric field on the effective dielectric constant. a_{pol} is obtained by fitting to an *ab-initio* molecular dynamic analysis [17]. $\epsilon_{eff}^{\nabla\phi=0}$ is the dielectric constant without electric field and is

defined as $\epsilon_{eff}^{\nabla\phi=0}(n_i) \coloneqq \epsilon_s^0 - \sum_{i=1}^{N}(n_i\,\beta_i/N_{avo})$, where β_i is the polarizability of solute i, ϵ_s^0 is the solvent's dielectric constant, and N_{avo} is the Avogadro's constant. The electrostatic potential at the bulk solution is set to zero. With these expressions of ω_{els}, $\delta\bar{\Omega}_{tot}/\delta\phi(x) = 0$ gives the Poisson equation with the effective dielectric constant ϵ_{eff} as described in Eq. S31 and S32 in the SI. In the bulk solution ($|\nabla\phi| \to 0, x > 0, n_i = n_i^0$), the effective dielectric constant becomes $\epsilon_{eff} = \epsilon_{eff}^{\nabla\phi=0}(n_i^0) = \epsilon_s^0 - \sum_{i=1}^{N}(n_i^0\,\beta_i/N_{avo})$. Hence, β_i can be obtained by measuring concentration dependent dielectric constant as $\beta_i = -N_{avo}\,d\epsilon_{eff}/dn_i^0$ [45] for the bulk solution.

2.3.3. Electron energy, ω_{elec}

This study employs electron energy to account for the effect of potential-dependent electron spillover. We employ a jellium model with uniform electron gas approximation [22] for its simple and low-cost computation. In the jellium model, positive charges in core atoms of the metal (n_m) are expressed as the uniform background charge, and the density distribution of the valence electrons ($n_e(x)$) is evaluated based on the kinetic and exchange-correlation energy of electrons with the mean-field approximation. Based on Smith's expression [29], our model evaluates the kinetic energy with the first-order density-gradient expansion, while it uses the local-density approximation for exchange-correlation energy. Because of the simplified interaction between the core electrons and the valence electrons, jellium models need modifications to improve their accuracy. Perdew et al. [32] introduced a structureless pseudopotential that represents the Madelung energy and the repulsive interaction from the core electrons. The accuracy of Perdew's model in predicting the work function and the bulk modulus of metals is, however, limited mainly because of the assumption of uniform background positive charge in the jellium model. The discrepancy becomes larger when the model is applied to transition and noble metals. Russier and Badiali

attributed the discrepancy on transition and noble metals to the contribution of d-electron [47]. To correct the errors, we employ the structureless pseudopotential in a semi-empirical manner. We employ two parameters in the model that are determined based on basic metal properties. One parameter, structureless pseudopotential [30, 32] (μ_{ps}^{m}), was determined from the bulk modulus of the metal (See Eq. S29 in SI). The other parameter, $\Delta\phi_{WF}$, was determined from the work function in vacuum and assumed to be independent of the electrode potential (See Section 2.5.1). We also assumed that the electrons that spill into the electrolyte phase feel a non-negligible potential due to the interaction with solvent molecules. This potential was expressed as the pseudopotential in the electrolyte phase. It was determined from the potential of zero charge of Ag (110) [48] and used as a constant value for other metals.

The grand potential for the electron energy is expressed as

$$\omega_{elec}(n_e, \nabla n_e, x) = \varepsilon_{elec}^{txc}(n_e, \nabla n_e) + \varepsilon_{elec}^{ps}(n_e, x) - n_e \mu_{elec}, \quad (15)$$

where ε_{elec}^{txc} is the summation of kinetic, exchange, and correlation energy of the electron based on Smith's expression [29]:

$$\varepsilon_{elec}^{txc}(n_e, \nabla n_e) \coloneqq \frac{e_{au}}{a_0^3}\left[\frac{3}{10}(3\pi^2)^{\frac{2}{3}} a_0^5 n_e^{\frac{5}{3}} - \frac{3}{4}\left(\frac{3}{\pi}\right)^{\frac{1}{3}} a_0^4 n_e^{\frac{4}{3}} - \frac{0.056 a_0^4 n_e^{\frac{4}{3}}}{0.079 + a_0 n_e^{\frac{1}{3}}} + \frac{a_0^5}{72}\frac{(\nabla n_e)^2}{n_e}\right], \quad (16)$$

where e_{au} is the Hartree energy and a_0 is the Bohr radius.ε_{elec}^{ps} is the structureless pseudopotential that takes different values in the metal ($x < 0$) and in the solution ($x > 0$),

$$\varepsilon_{elec}^{ps}(n_e, x) \coloneqq n_e\left(\mu_{ps}^{m}\Theta(-x) + \mu_{ps}^{s}\Theta(x)\right), \quad (17)$$

where μ_{ps}^{m} and μ_{ps}^{s} are the pseudopotentials in the metal and solution, respectively. μ_{elec} is the chemical potential of the electron and is defined as

$$\mu_{elec} \coloneqq -e_0(E_{WE} - \Delta\phi_{WF}), \tag{18}$$

where E_{WE} is the absolute potential of the working electrode and $\Delta\phi_{WF}$ is a constant used to correct the potential to match the vacuum work function. E_{WE} is a control parameter in the calculation.

2.3.4. Solute-solute interaction, ω_{ss}

We account for the electrostatic solute-solute interactions by assuming that the solvation shells prevent the solutes from getting close to other solute molecules to feel chemical interactions. Although the electrostatic interaction (ω_{els}) accounts for the electrostatic interaction along the x direction; it does not include the interaction in $y-z$ plane because it is a 1-dimensional model. Ions in the solution interact with each other and redistribute due to the electrostatic interaction, which affects the total energy. This $y-z$ plane electrostatic interaction is accounted for as solute-solute interaction. The solute-solute interaction is obtained by analytically solving the Poisson-Boltzmann equation. The governing equations are the same as that of Debye-Hückel theory; however, we used a cylindrical coordinate in $y-z$ plane, instead of spherical coordinates, to avoid double counting electrostatic interactions in the x direction. The interaction is thus expressed in the form of

$$\omega_{ss}(n_i) = \varepsilon_{ss}^{ion}(n_i) - \sum_{i=1}^{N} n_i z_i^2 \mu_{ss}^{ref}\,, \tag{19}$$

where ε_{ss}^{ion} is the ion-ion interaction in $y-z$ plane and μ_{ss}^{ref} is the reference chemical potential expressed as

$$\varepsilon_{ss}^{ion}(n_i) \coloneqq -\frac{k_B T}{4\pi r_{ave}^3}\left[\ln\left(\frac{\pi}{2} j x_{ss} Y_1\left(j x_{ss}(n_i)\right)\right) + \frac{1}{2}\left(x_{ss}(n_i)\right)^2\right], \tag{20}$$

$$\mu_{ss}^{ref} \coloneqq \frac{e_0^2}{8\pi\epsilon_0\epsilon_{eff}^0 r_{ave}}\left(\frac{real\left(Y_0\left(j x_{ss}(n_i^0)\right)\right)}{real\left(j x_{ss}(n_i^0) Y_1\left(j x_{ss}(n_i^0)\right)\right)} - 1\right), \tag{21}$$

where r_{ave} is the average radius of the solute molecules, j is the imaginary unit. Y_0 and Y_1 are the Bessel function of the second kind of order 0 and order 1, respectively. x_{ss} is an intermediate variable described by $x_{ss}(n_i) \coloneqq \left[e_0^2 r_{ave}^2 (\sum_{i=1}^N z_i^2 n_i)/\left(\epsilon_0\epsilon_{eff}^0 k_B T\right)\right]^{0.5}$. In the derivation of this expression, we employed the first-order approximation of $|z_i e_0 \phi / k_B T| \ll 1$. Although this approximation becomes less accurate when the ion effective radius is small, it enables analytic expression, which is needed to include the effect of y-z direction distribution in the 1-dimensional grand potential, ω_{tot}. This interaction is newly introduced in this model, whose derivation is shown in Section S2.2 in SI.

2.3.5. Wall-Solute/solvent interaction, ω_{ws}

To simplify the analysis, this work focuses on a system without significant specific interaction between the electrode and solute or solvent. Hence, in this study, ω_{ws} only accounts for solute ions' steric restriction for closest approach due to their finite size:

$$\omega_{ws}(n_i, x) = \sum_i n_i \mu_{ws,i}(x), \tag{22}$$

where $\mu_{ws,i}$ is the chemical potential for wall-solute/solvent interactions and is defined as $\mu_{ws,i} \coloneqq \mu_{cut}\Theta(r_i - x)$. μ_{cut} is the cut off chemical potential (set to 1000 eV), and r_i is the species' effective radius.

2.4. Boundary conditions

Since the problem to be solved is 1-dimensional with physics described by second-order differential equations, we need two boundary conditions for each variable. For electrostatic potential, the boundary conditions are set as $\phi(L_{sol}) = 0$ and $\nabla\phi(-L_{metal}) = 0$. For electron density, $n_e(L_{sol}) = 0$ and $n_e(-L_{metal}) = n_e^0$. From the definition of reference energy, $\nabla n_e(L_{sol}) = \nabla n_e(-L_{metal}) = 0$ is satisfied when L_{slv} and L_{metal} are large enough. For species' density n_i, the boundary conditions are $\nabla n_i(L_{sol}) = \nabla n_i(0) = 0$, which automatically satisfies $n_i(L_{sol}) = n_i^0$ because of the definition of the reference energy. With these boundary conditions, the working electrode (E_{WE}) was controlled to estimate how the system reacts to the electrode potential change.

2.5. Parameter setting

Here we describe the parameter setting protocols for electrode or electrolyte specific parameters. The values of the parameters for the electrode and electrolyte are tabulated in Table 1 and Table 2, respectively.

2.5.1. Electrode specific parameters

The model uses three electrode-specific experimental properties: the Wigner-Seitz radius (r_{ws}) [49], the bulk modulus (B) [33 50], and work function in the vacuum (Φ_{vac}^{exp}) [51-53]. The Wigner-Seitz radius is employed to evaluate the electron density in the bulk metal, $n_e^0 \coloneqq 3/(4\pi r_{ws}^3)$. The bulk modulus is used to estimate the pseudopotential in the metal (μ_{ps}^m) using the relation of $B = V(\partial^2 E/\partial V^2)_N$, where V, E, and N are the volume, energy, and number of electrons in the metal (see Section S2.3 in SI). $\Delta\phi_{WF}$ was assumed to be a constant and was determined from the work function in vacuum as $\Delta\phi_{WF} = \Phi_{vac}^{exp} - \Phi_{vac}^{calc}$, where Φ_{vac}^{exp} is the experimental work function and Φ_{vac}^{calc} is the calculated work function when $\Delta\phi_{WF} = 0$. In the calculation of work function in vacuum, we set the effective dielectric constant to be 1, species' density n_i to be 0, and pseudopotential outside of the metal to be 0.

2.5.2. Electrolyte-specific parameters

The model employs six electrolyte-specific properties: the ionic valence of anion and cation (z_a and z_c), effective hydrated radius of anion and cation (r_a and r_c), and the polarizability of the hydrated shell of anion and cation (β_a and β_c). z_i is obtained from the ionic formula. $\beta_i\left(\coloneqq d\epsilon_{eff}/dc_i\right)$ is from the experimental results for concentration-dependent dielectric potential [45]. r_i is calculated from the distance between the ion's center and center of the nearest water molecule [54], including up to the first water layer for anions and second water layer for cations [55]. The electrons' pseudo-chemical potential in the solvent (μ_{ps}^s) is also needed to be determined using an experimental result. We employed the potential of zero charge (PZC) on Ag(110) in 5 mM NaF (–0.731 V vs SHE [48]) to get μ_{ps}^s=–0.043 eV. We fixed this value for all the calculations using aqueous electrolyte because we assume that it stems from the interaction between the electron from

metal and the water molecules [36]. In the calculation, the absolute potential for standard hydrogen electrode (SHE) is set as 4.44 V [56].

Table 1. Input properties of the electrodes

	r_{ws} /a.u.	B /Mbar	Φ_{vac}^{exp} /eV
Ag (110)	3.01 (Ref [49])	1.01 (Ref [33])	4.14 (Ref [51])
Pt (111)	2.90 (Ref [49])	2.78 (Ref [33])	5.93 (Ref [52])
Hg	3.10 (Ref [49])	0.267 (Ref [50])	4.48 (Ref [53])

The calculated value for $\Delta\phi_{WF}$ to satisfy the vacuum work function (Φ_{vac}^{exp}) are: 1.40 V, 3.01 V, and 1.32 V for Ag (110), Pt (111), and Hg, respectively.

Table 2. Input properties of the electrolyte

	r_i /nm (Ref [54]) *	β_i /M^{-1} (Ref [45])	z_i
Na^+	0.65	7	+1
K^+	0.69	10	+1
F^-	0.40	3	-1
ClO_4^-	0.51	1	-1

*: For anions, only the first hydration shell was included, while second hydration shell was included for cations assuming the stronger hydration affinity of cations [55]. For water radius, 0.138 nm was used [54].

3. RESULTS AND DISCUSSIONS

3.1. Evaluation of the calculated results

The model calculates the distribution of ϕ, n_e, and n_i (cations: i=c, anions i=a) at the given electrode potential (E_{WE}) as shown in Figure 1. The material specific parameters are tabulated in Table 1 and 2. The electrostatic potential (ϕ) increases under higher electrode potential, while the electron density (n_e) in the electrolyte phase decreases for higher E_{WE}. The anion density (n_a) is higher when higher potential is applied, while the opposite trend is observed for cations (n_c). The anion and cation density decrease to almost zero respectively at $x \leq 0.51$ nm and $x \leq 0.65$ nm because of the steric wall-solute interaction (ω_{ws}) defined in Eq. 22, corresponding to the Stern

layer. These trends are physically representative and reasonably consistent with the previous analyses for the EDLs [8, 9, 20]. By integrating the charge density of ions in the electrolyte phase, one can obtain the surface charge density σ_{ion}:

$$\sigma_{ion} \coloneqq \int_0^{L_{sol}} e_0\big(z_a n_a(x) + z_c n_c(x)\big)\, dx\,, \tag{23}$$

When L_{sol} and L_{metal} are large, the total charge density $\sigma_{tot} \coloneqq \sigma_{ion} + \sigma_{metal}$ becomes zero, where

$$\sigma_{metal} \coloneqq \int_0^{L_{sol}} e_0\big(n_e^0 \Theta(-x) - n_e(x)\big)\, dx\,, \tag{24}$$

The first term in the parentheses represents the positive background charge in the metal. At potential of zero charge (PZC), $\sigma_{ion} = \sigma_{metal} = 0$. For comparison with the experiment, the differential capacitance, C_d, was calculated by taking the derivative of σ_{ion} with respect to the electrode potential:

$$C_d = \frac{d\sigma_{metal}}{dE_{EW}} = -\frac{d\sigma_{ion}}{dE_{EW}}, \tag{25}$$

The differential capacitance is experimentally measurable with EIS or CV by using the relation of $d\sigma_{ion}/dt = -I$, where I is the current (positive current means oxidation current). The surface-charge density and differential capacitance are shown in Figure 2. The surface-charge density is positive below the PZC and negative above the PZC. In the varied potential range, the surface-charge density is monotonic. The double-layer capacitance exhibits a local minimum at the PZC because this is where the interface is least charged, then there are two humps below and above

PZC that are not symmetric. This asymmetry arises from anions being smaller in effective hydrated radius compared to the cations, which is discussed in Section 3.3.

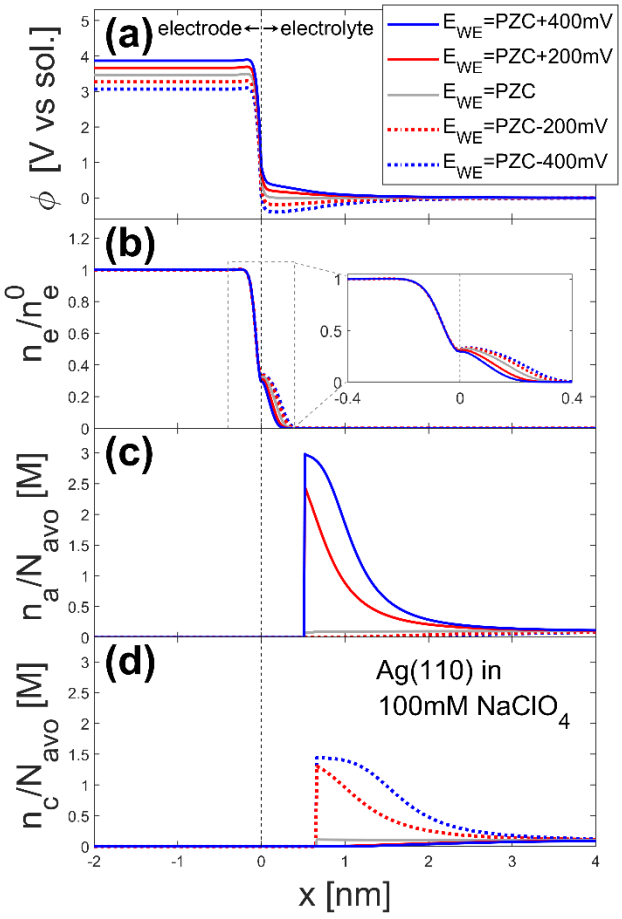

Figure 1. Calculated distributions of (a) electrostatic potential (ϕ), (b) electron-density (n_e), (c) anion-density (n_a), and (d) cation-density (n_c) for Ag (110) in 100 mM $NaClO_4$. The horizontal axis shows the position in x direction ($x < 0$ is in the electrode phase and $x > 0$ is in the electrolyte phase) and the different line styles represent different electrode potentials as shown in the legend in (a). The insert in (b) is the enlarged view of the domain inside the gray dashed box.

N_{avo} is the Avogadro number. The black dashed line indicates the interface between the electrode ($x < 0$) and the electrolyte ($x > 0$).

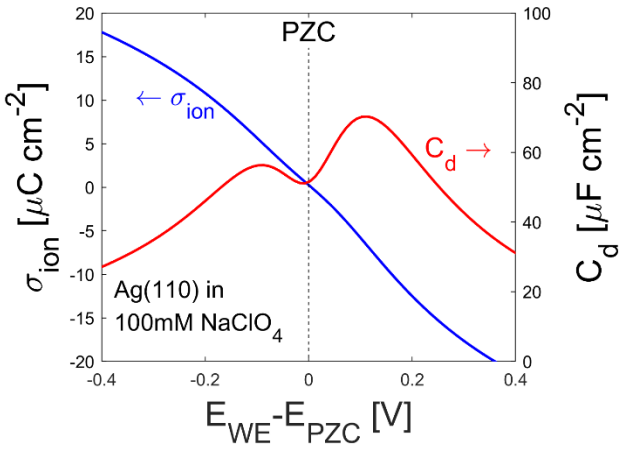

Figure 2. Calculated surface-charge density of ions (σ_{ion}, blue line, left axis) and differential capacitance, (C_d, red line, right axis) with respect to the electrode potential (E_{WE}). The parameter set for Ag (110) in 100 mM $NaClO_4$ is used. The black dashed line corresponds to the potential of zero charge (PZC). σ_{ion}, E_{WE}, and E_{PZC} represent the surface charge in the electrolyte (Eq. 23), the working electrode potential, and the PZC, respectively.

3.2. Comparison with experimental results

At first, we analyzed Ag (110) in NaF and $NaClO_4$ electrolytes and compared the differential capacitance predicted by the model with the experimental results by Valette [48], whose analysis suggests the effect of specific ion adsorption in this system is not significant. Figure 3 (a) and (b) show that our model captures the trends in the experiments: the differential capacitance has two local maxima and one local minimum. The local minimum increases when the ion concentration

increases, and the height of the first local maximum (–0.9 to –0.8 V vs SHE), in the potential range below the PZC, is almost the same for $NaClO_4$ and NaF, while the second local maximum (–0.65 to –0.55 V vs SHE), above the PZC, depends strongly on anion species identity. Because the first local maximum can be attributed to cation adsorption (when the metal is negatively charged) and the second one is due to anion adsorption (when the metal is positively charged; see section 3.5.), the change in the anion species only affects the second local maximum. The calculated height of the maxima and minima also agrees well with the experiment. Overall, the calculated results demonstrate good agreement with the experimental ones for all the electrolyte concentration and species without parameter fitting, suggesting the predictivity of the model.

Next, we checked the model applicability to different electrodes. As a system without significant specific adsorption, we calculated the differential capacitance on Hg in NaF solutions and compared it with the experimental results by Grahame [57], whose analysis suggests the specific ion adsorption is not significant in this system. The comparison between calculation and experimental results are shown in Figure 3(c). Although the agreement is not perfect, the calculation successfully reproduces the different features of Hg compared to Ag: lower differential capacitance with significantly suppressed capacitance maxima. Considering that the model does not use any adjustable parameters, the agreement is satisfactory. The quantitative discrepancy between the experiment and calculation for Hg can probably be attributed to water chemisorption on Hg [58], which is not accounted for in the present model.

The difference in C_d between Ag (110) and Hg can be attributed to the difference in the stability of electrons in the metals. In our model, the metal bulk modulus is associated with the pseudopotential of electrons in the metal. Here, the bulk modulus of Hg is 0.267 Mbar [50], while that of Ag is 1.01 Mbar [33]. As described in Eq. S29 in SI, larger bulk modulus results in higher

pseudopotential in the metal because of stronger repulsive interactions from the core electrons. With higher pseudopotential, the electrons become less stable in the metal and the electron-density profile ($n_e(x)$) becomes more sensitive to the applied electrode potential (compare Fig. 1(b) and Fig. 4(a)). The larger sensitivity of $n_e(x)$ on E_{WE} results in larger $d\sigma_{metal}/dE_{WE}$, which equals C_d (Eq. 25). When we focus on the Helmholtz capacitance (C_H), the difference between the two electrodes becomes clearer as shown in Fig. 4 (b). Here, C_H is calculated by

$$C_H = \frac{d\sigma_{metal}}{d\big(\phi(-L_{metal}) - \phi(L_{zeta})\big)}, \tag{26}$$

where $L_{zeta} = \min(r_a, r_c)$ is the closest approach of ions.

Also, we compared the calculated differential capacitance on Pt(111) in 100 mM $KClO_4$ with the experimental result by Pajkossy and Kolb [4] to check the model applicability to a system with specific adsorption [59, 60]. Figure 3(d) shows the results for Pt(111) electrode. The figure shows a significant discrepancy between the experiment (the solid line) and the calculation (the dotted line) in terms of peak height, location, and number of peaks. The discrepancy is thought to be due to the specific interaction between Pt(111) surface and ClO_4^- ion [59], which can be corrected by using an appropriate function for chemical potential for wall-anion interaction ($\mu_{ws,a}$) (see the dash-dotted line in Fig. 3 (d)). Here we used the form of Morse potential as

$$\mu_{ws,a}(x) = G_{ads}\left\{e^{2\alpha_1(r_a^{ads}-x)} - 2e^{\alpha_1(r_a^{ads}-x)}\right\}, \tag{27}$$

where, G_{ads} is the adsorption free energy (0.65 eV), α_1 is the relaxation parameter (4.72 nm^{-1}), and r_a^{ads} is the effective radius of adsorbed anions (0.4 nm). Also, we accounted for the anion hydrated radius shift as $r_a(x) = r_a^0 + (r_a^{ads} - r_a^0)\Theta\Big(x - 0.5(r_a^0 + r_a^{ads})\Big)$, where r_a^0 is the effective anion radius in the bulk solution. Because of the lack of quantum-mechanical analysis

(e.g., DFT calculation) on this interaction, we cannot conclude that the assumed interaction is physically reasonable. However, this result confirmed that the ion-electrode specific interaction can significantly alter the differential capacitance and needs to be accounted for when applying the model to a system with specific adsorption. Also, it should be noted that quantum-mechanical analysis can be used to assess the significance of the specific interaction term in a certain system in case sufficient experimental data is unavailable. By running a DFT simulation with various ion-metal surface distance, one can obtain a free energy profile. This profile can serve as the wall-solute interaction term ($\mu_{ws,a}(x)$) in a similar manner as Eq. 27. If the adsorption free energy is sufficiently large, it will affect the calculated differential capacitance, which suggests the importance of including specific interaction term in the model.

It is known that water molecules form a 2-dimensional hydrogen bonding network on electrode surface like platinum [15] that stabilize the water molecules and change their dielectric properties [11-13]. Although our model includes the polarization energy that accounts for the stabilization of solvent dipole for the electric field, it does not include the explicit expressions for the 2-dimensional hydrogen bonding in the vicinity of the interface. The model will be capable of including these effects by setting the parameters based on further analyses. The former effect, stabilization of water, prevents solute molecules from approaching the surface. This blocking effect can be included by obtaining the wall-solute interaction energy (μ_{ws}) from DFT calculations with explicit water molecules, which evaluates the energy to put the solute molecule near the interface, including the reorganization energy of water hydrogen bond. Also, the latter effect, change in the dielectric properties, can be implemented by making the dielectric parameters (*e.g.* ϵ_s^0 and a_{pol}) position dependent. However, this analysis is beyond the scope of current study and requires parameter fitting that are not readily available and/or are computationally cost prohibitive.

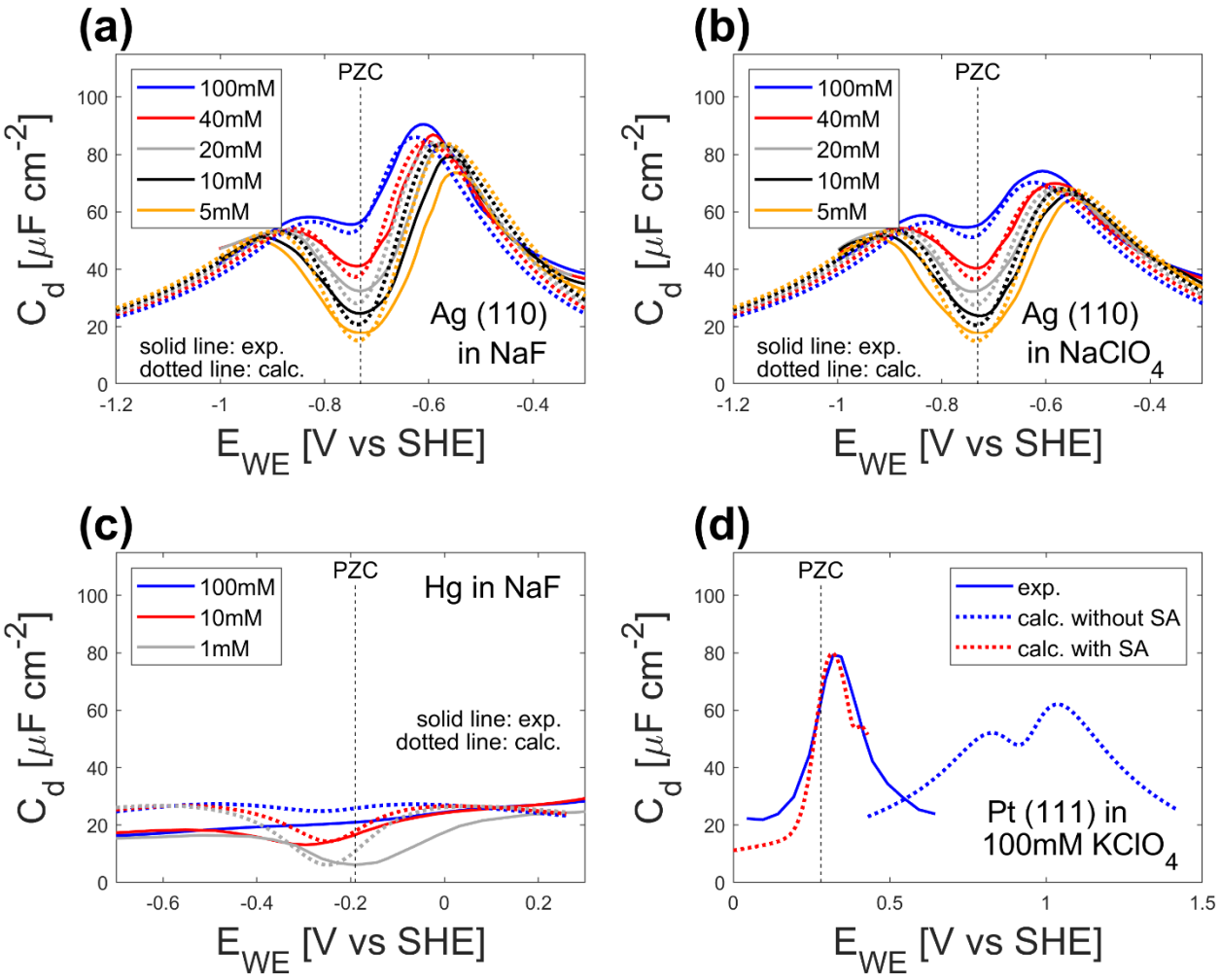

Figure 3. Comparison between the calculated (dotted lines) and experimental (solid lines) differential capacitance; (a) Ag (110) in NaF, (b) Ag (110) in $NaClO_4$, (c) Hg in NaF, and (d) Pt (111) in 100 mM $KClO_4$ (solid blue line: experimental, dotted blue line: calculated without specific interaction, dotted red line: calculated with specific interaction (Eq. 27)). Experimental results for (a) and (b) are extracted from ref [48], data for (c) are from ref [57], and data for (d) are from ref [4]. The black dashed lines indicate the potential of zero charge (PZC).

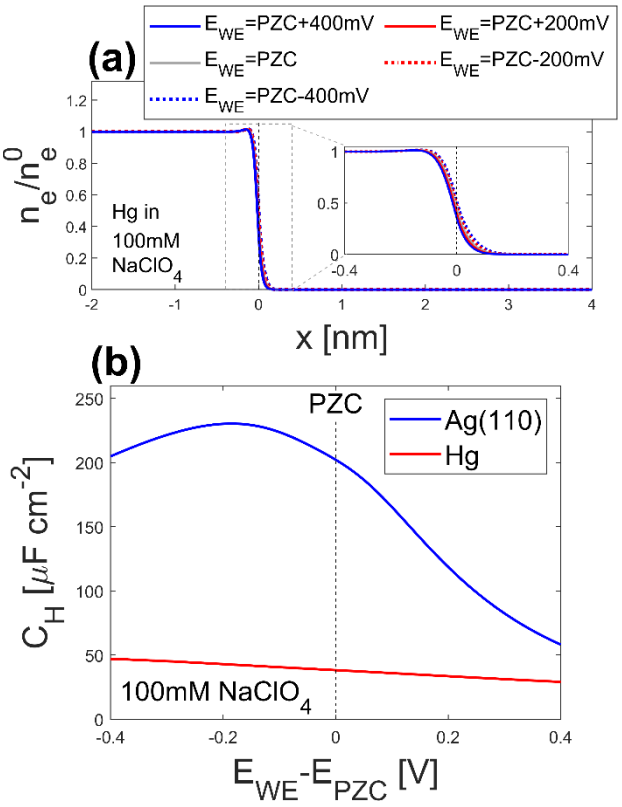

Figure 4. Calculated (a) electron density distributions on Hg in 100mM $NaClO_4$ and (b) the Helmholtz capacitance (Eq. 26) of Hg (blue) and Ag (110) (red) electrodes in 100mM $NaClO_4$ (b). For (a), the axis and the line styles are the same as that in Fig. 1 (b). The insert in (a) is the enlarged view of the domain inside the gray dashed box. The black dashed lines in (a) and (b) indicate the electrode – electrolyte interface and potential of zero charge (PZC), respectively.

3.3. Effect of grand-potential components

The effect of each grand-potential component is analyzed by enabling them one by one in the calculation for Ag(110) in 100 mM NaF by substituting the total local grand potential (ω_{tot}) in Eq. 5 with $\omega_{tot}^{(k)}$ in Table 3.

The initial model ($\omega_{tot}^{(1)}$) corresponds to standard GCS theory. It accounts for the ideal mixing entropy (ε_{mix}^{id}), electrostatic energy (ω_{els}), and wall-solute interaction (ω_{ws}). Since the electron energy (ω_{elec}) is missing in this model, the partial derivative of ω_{tot} with n_e and ∇n_e in Eq. 5 does not provide any meaningful information. Hence, instead of solving for the differential equation for n_e, we manually set $n_e(x) = n_e^0\Theta(-x)$, which results in neglecting the effect of the surface dipole due to electron spillover. This model also neglects the dielectric saturation due to the polarization of the solvent and solutes by setting $a_{pol} \to 0$. In addition to it, the solute molecules are assumed to have the same size to exclude the effect of ion size differences. The second model ($\omega_{tot}^{(2)}$) corresponds to the Bikerman model [19], which accounts for the effects of finite size of solute ions on mixing entropy (ε_{mix}^{slv}) by assuming all ions have the same size. The third model ($\omega_{tot}^{(3)}$) adds the electron energy term (ω_{elec}) to the second model that enables the evaluation of $n_e(x)$, which corresponds to the density-potential functional theory developed by Huang [20]. The fourth model ($\omega_{tot}^{(4)}$) activates the dielectric saturation by setting $a_{pol} = 6$ nm/V, a fitted value to an *ab-initio* simulation result [17]. The fifth model ($\omega_{tot}^{(5)}$) enables the solute-solute interaction (ω_{ss}) to visualize its effect on the calculation results. Finally, the sixth model ($\omega_{tot}^{(6)}$) includes the effect of ion size difference between anions and cations on the mixing entropy by activating ε_{mix}^{size} and setting $r_a \neq r_c$.

Table 3. Expressions for $\omega_{tot}^{(k)}$ to analyze the effects of the grand potential components.

Expression for $\omega_{tot}^{(k)}$	r_a [nm]	r_c [nm]	a_{pol} [nm/V]
$\omega_{tot}^{(1)} \coloneqq \varepsilon_{mix}^{id} - \sum_{i=1}^{N} n_i \mu_{mix,i} + \omega_{els} + \omega_{ws}$	0.65	0.65	$\to 0$
$\omega_{tot}^{(2)} \coloneqq \varepsilon_{mix}^{id} + \varepsilon_{mix}^{slv} - \sum_{i=1}^{N} n_i \mu_{mix,i} + \omega_{els} + \omega_{ws}$	0.65	0.65	$\to 0$
$\omega_{tot}^{(3)} \coloneqq \varepsilon_{mix}^{id} + \varepsilon_{mix}^{slv} - \sum_{i=1}^{N} n_i \mu_{mix,i} + \omega_{els} + \omega_{elec} + \omega_{ws}$	0.65	0.65	$\to 0$
$\omega_{tot}^{(4)} \coloneqq \varepsilon_{mix}^{id} + \varepsilon_{mix}^{slv} - \sum_{i=1}^{N} n_i \mu_{mix,i} + \omega_{els} + \omega_{elec} + \omega_{ws}$	0.65	0.65	6
$\omega_{tot}^{(5)} \coloneqq \varepsilon_{mix}^{id} + \varepsilon_{mix}^{slv} - \sum_{i=1}^{N} n_i \mu_{mix,i} + \omega_{els} + \omega_{elec} + \omega_{ss} + \omega_{ws}$	0.65	0.65	6
$\omega_{tot}^{(6)} \coloneqq \omega_{mix} + \omega_{els} + \omega_{elec} + \omega_{ss} + \omega_{ws}$	0.40	0.65	6

For k = 1 and 2, the electron density is set as $n_e(x) = n_e^0 \Theta(-x)$.

Figure 5 shows that $\omega_{tot}^{(1)}$ gives the differential capacitance with one local minimum, which saturates when the potential is far from the PZC as expected from GCS theory. The line for $\omega_{tot}^{(2)}$ shows that the addition of ε_{mix}^{slv} results in the two local maxima, suggesting that they are due to the ions' finite size. ε_{mix}^{slv} impacts the capacitance far from the PZC because the limited availability of the space for solvent near the interface mitigates further ion accumulation. The line for $\omega_{tot}^{(3)}$ shows that the electron energy (ω_{elec}) increases the capacitance around PZC, and the effect is more significant in negative potential vs PZC than in positive potential. This is because the electron spillover becomes more significant in negative potential, where the electron is relatively unstable in the electrode (thus the Helmholtz capacitance C_H becomes larger in negative potential as shown in Fig. 4 (b)); this result is consistent with the discussion by Huang [20]. The polarization of solvent and solute ions ($a_{pol} \neq 0$) reduces the differential capacitance in the potential far from the PZC (the line for $\omega_{tot}^{(4)}$). This is because the polarization of the ions and solvents induces dielectric saturation, which reduces the effective dielectric constant near the interface and thus the Stern-

layer capacitance when the electric field is strong [16]. The addition of solute-solute interaction (ω_{ss}) slightly increases the height of the peak (the line for $\omega_{tot}^{(5)}$) because of the favorable interactions between the ions in higher ion strength. Although the effect of this interaction is not significant in case of monovalent electrolyte, it becomes larger as the ionic valence increases (see Fig. S1 in SI). The line for $\omega_{tot}^{(6)}$ shows increased differential capacitance especially above the PZC. This is because the smaller size of anion enhances the anion accumulation near the interface. Another analysis of the effects of the interaction terms, which uses a different order, also demonstrate significant effects of polarization of solvent and solute ions, as well as the size-dependent entropy (see Fig. S2 in SI). This analysis suggests that all the interactions introduced in this study, polarization of solvent and solute ions, size-dependent entropy, and solute-solute interactions, are responsible for predicting differential capacitance.

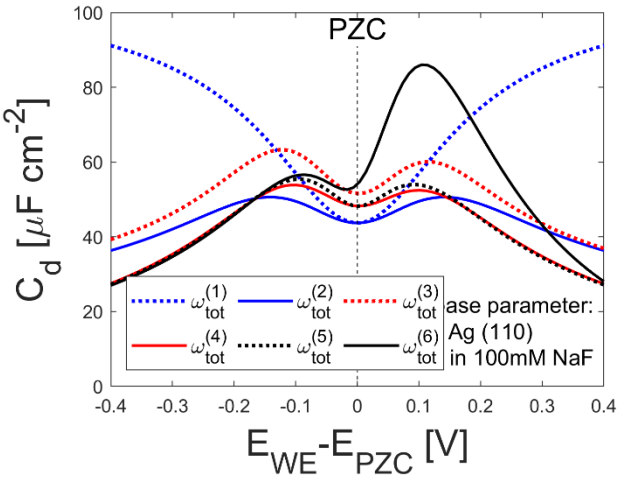

Figure 5. Comparison of calculated differential capacitance with $\omega_{tot}^{(i)}$: The different line styles represent different expressions for ω_{tot} as shown in the legend. The parameter set for Ag (110) in 100 mM NaF was used as the base parameters.

3.4. Parameter sensitivity

Parameter sensitivity analysis is conducted with the model to identify the critical material properties that impact the EDL structure. The parameters to be analyzed are the material properties introduced in Section 2.5: the effective hydrated radius of anion and cation (r_a and r_c), polarizability of the hydrated shell of anion and cation (β_a and β_c), ionic valence of anion and cation (z_a and z_c), the Wigner-Seitz radius of the electrode (r_{ws}), the bulk modulus of the electrode (B), and vacuum work function of the electrode (Φ_{vac}). By changing these material properties by $\pm$5% independently from the base parameters (values on Ag(110) in 100 mM NaF), we evaluated 4 properties of EDL structures: PZC (E_{PZC}), C_d at E_{PZC}, C_d at $E_{PZC} - 0.1\text{V}$, and C_d at $E_{PZC} + 0.1\text{V}$. The difference of $\pm$5% is chosen as a value small enough to obtain a numerical derivative and large enough to neglect the effect of the numerical error due to solver tolerance. Then the sensitivity of EDL property k on the material property j ($S_{k,j}$) was calculated by

$$S_{k,j} \coloneqq m_j\left(\Delta e_{k,j}/\Delta m_j\right), \tag{28}$$

where m_j is the base value of the material property j, $\Delta e_{k,j}$ is the shift of the EDL property k due to the shift in the material property j, and Δm_j is the shift in the material property j. The calculated sensitivities of the EDL properties on the material properties are shown in Fig. 6.

First, the effects of the electrolyte properties, r_a, r_c, β_a, β_c, z_a, and z_c are discussed. Figure 6 demonstrates that none of these parameters have a recognizable effect on PZC, which confirms that PZC is independent of electrolyte properties in this model of no specific interactions. The properties of the anion (r_a, β_a, and z_a) mainly affect $C_d(E_{PZC} + 0.1\text{V})$, while the properties of the

cation (r_c, β_c, and z_c) show similar effects but in $C_d(E_{PZC} - 0.1\text{V})$. Above the PZC, the anion accumulates near the interface (Fig. 1 (c)). Since the anion properties affect the anion's accumulation affinity, they can impact the surface charge profile and thus the differential capacitance in high potential. The cation, on the other hand, accumulates under the PZC (Fig. 1 (d)) and thus the cation properties have stronger effects on the differential capacitance in negative potential. The calculation results show that the electrolyte properties: r_a, r_c, z_a, and z_c have large effects on the differential capacitance. Hence, one needs to take care of the effective ion radius and ionic valence to control the EDL structures.

In terms of sensitivity of the electrode properties: r_{ws}, B, and Φ_{vac}, Figure 6 demonstrates that r_{ws} has a strong effect on all EDL properties. This strong effect can be attributed to the third-order effect of r_{ws} on n_e^0 ($n_e^0 \coloneqq 3/(4\pi r_{ws}^3)$) and the impact of n_e^0 on the electron spillover (see the shift from $\omega_{tot}^{(2)}$ to $\omega_{tot}^{(3)}$ in Fig. 5). Φ_{vac} significantly changes the PZC but no recognizable effects on differential capacitance. In this model, Φ_{vac} is used to evaluate $\Delta\phi_{WF}$, which is a constant that simply shifts the absolute potential of the electrode. The shift in the absolute potential directly changes the PZC but does not change the shape of potential-dependent differential capacitance. The bulk modulus (B) affects all of the EDL properties, but the impact is smaller than r_{ws}. Even with the small sensitivity, it was the main reason for the difference between Ag(110) and Hg as discussed in Section 3.2. because of the large difference in the bulk modulus (1.01 Mbar for silver [33] and 0.267 Mbar for mercury [50]). The positive sensitivity of C_d on B is consistent with the smaller C_d on Hg than on Ag (110). Although the Wigner-Seitz radius is the most sensitive property of the electrode, one needs to also consider the bulk modulus to predict the differential capacitance.

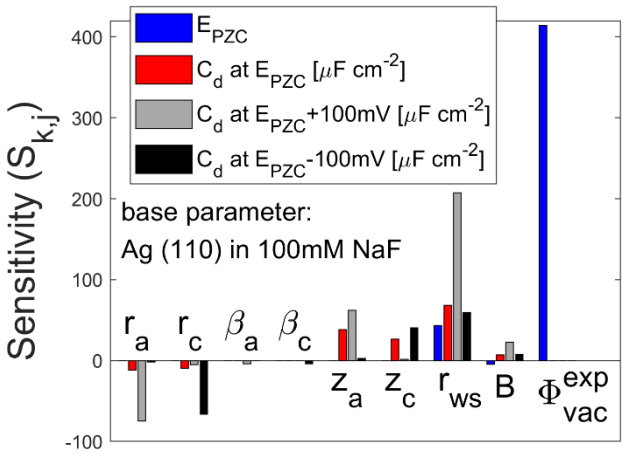

Figure 6. Sensitivity (Eq. 28) of EDL properties on the material properties. The different colors represent different material properties as listed in the legend. The parameter set for Ag (110) in 100 mM NaF is used as the base parameters.

3.5. Potential applications of the model

Since this model provides a means to predict the structure of EDLs without parameter-fitting, it can be applied in various applications including different materials and reaction microenvironments, whereas conventional continuum EDL models require parameter fitting based on the experimental results. For example, Huang's model [20] calibrates the optical dielectric constant based on the experimental differential capacitance. Since the model presented herein does not require parameter-fitting, it can be used to predict the EDL structure without experimental data, which gives us the insights on material selection to control the surface properties.

Also, the continuum descriptions developed in this study can be extended into higher dimensions to address the inhomogeneous nature of the electrode surface, which plays a significant role in electrocatalytic processes [15]. To fully account for the inhomogeneity of the interface, the

model can be extended into 3-dimensional space and then coupled with quantum mechanical simulations by incorporating the present model as an implicit solvent model in DFT simulations [27, 61-64]. The present model would improve the accuracy of DFT simulations by providing a more accurate description of interactions in the electrolyte. Although our model might increase the computational cost due to the need for iterative calculations for solute molecule distributions (n_i), it would improve the calculation accuracy of implicit water model because of the improved descriptions in the size dependent entropy term and the polarization model. One should note that in this application, the calculation becomes 3-dimensional so that we no longer need to include the solute-solute interaction (ω_{ss}), which is derived by integrating the Coulomb interaction in the y-z direction.

4. CONCLUSIONS

In this study, a predictive multiscale continuum model was developed for the electric double layer that eliminates the need for parameter fitting due to the use of incorporation of microscopic interactions and independent material properties. The model reproduced the trends in the experimental differential capacitance with multiple non-interacting electrode and electrolyte materials (Ag(110) in NaF, Ag(110) in $NaClO_4$, and Hg in NaF), which verifies the accuracy and predictiveness of the model. However, the poorer predictions for Pt(111) in $KClO_4$ suggest the necessity of further study to capture the effect of electrode-ion specific interactions in a parameter-fitting-free manner. The difference in the differential capacitance between Hg and Ag(110) was attributed to the difference in the electron stability in the metal. Sensitivity analyses confirmed that all the newly incorporated interactions added in this study play a role in predicting the differential capacitance. It also demonstrated the effective ion radius, the ionic valence, the electrode's

Wigner-Seitz radius, and the bulk modulus of the electrode are significant material properties that control the EDL structure. The model framework and findings provide insights into the EDL structures and enable predictiveness with low computational cost.

ASSOCIATED CONTENT

Supporting Information.

The Supporting Information is available free of charge.

List of equations and parameters (Table S1 – S3), Derivation of the equations, PDE expressions, and additional calculation results (Figure S1 and S2). (PDF)

AUTHOR INFORMATION

Corresponding Author

Masao Suzuki Shibata; orcid.org/0000-0001-5584-4938; Email: masaos@lbl.gov

Co-corresponding Authors

Adam Z. Weber; orcid.org/0000-0002-7749-1624; Email: azweber@lbl.gov

Iryna V. Zenyuk; orcid.org/0000-0002-1612-0475; Email: iryna.zenyuk@uci.edu

Author Contributions

M.S.S. developed the theory, constructed the model, performed calculations, summarized findings, and drafted the manuscript. Y.M., I.V.Z., and A.Z.W. provided guidance throughout the research

process, including literature survey, theory development, summarizing results, and manuscript preparation. Additionally, I.V.Z. provided an initial model for the study.

ACKNOWLEDGEMENTS

This work was partially supported by the Hydrogen and Fuel Cell Technologies Office (HFTO), Office of Energy Efficiency and Renewable Energy, U.S. Department of Energy (DOE) through the Million Mile Fuel Cell Truck (M2FCT) consortia, technology managers G. Kleen and D. Papageorgopoulos, and a CRADA with Toyota Central R&D Labs., Inc. Additionally, this work was supported by the DOE Office of Science Energy Earthshot Intiatives as part of the Center for Ionomer-based Water Electrolysis at Lawrence Berkeley National Laboratory under contract number DE-AC02-05CH11231. Also, the authors are thankful to Dr. Ryosuke Jinnouchi in Toyota Central R&D Labs., Inc. for fruitful discussions on microscopic interactions in the double-layer structure.

NOMENCLATURE

CONSTANTS

a_0 Bohr radius (5.292×10^{-11} m)

a_{pol} Constant for dielectric saturation of water (6.0×10^{-9} m/V)

e_0 Elementary charge. (1.602×10^{-19} C)

e_{au} Hartree energy (4.360×10^{-18} J)

j Imaginary unit ($\sqrt{-1}$).

k_B Boltzmann constant. (1.381×10^{-23} J/K)

N_{avo} Avogadro's constant (6.022×10^{23} 1/mol)

T Temperature of the system. (298 K)

ϵ_0 Vacuum permittivity (8.854×10^{-12} F/m)

ϵ_s^0 Solvent's dielectric constant (80.1)

ϵ_{op}^m Optical dielectric constant of the metal (1.00)

ϵ_{op}^s Optical dielectric constant of the solvent (1.76)

μ_{cut} Cut off chemical potential (1.0×10^3 eV=1.602×10^{-16} J)

MATERIAL PROPERTIES

B Bulk modulus (Table 1, Ref [33 50])

r_i Effective radius of solute i (Table 2, Ref [54, 55])

r_{ws} Wigner-Seitz radius (Table 1, Ref [49])

z_i Ionic valency of solute i (Table 2)

β_i Polarizability of solute i ($\beta_i \coloneqq -N_{avo}\, d\epsilon_{eff}^0/dn_i^0$) (Table 2, Ref [45])

Φ_{vac}^{exp} Experimental work function (Table 1, Ref [51-53])

CONTROLED VARIABLES

c_i^0 Concentration of solute i in the bulk electrolyte ($\sum_{i=1}^{N} z_i c_i^0 = 0$)

E_{WE} Absolute potential of the working electrode

INDEPENDENT VARIABLES

n_e Electron number density. ($n_e(L_{sol}) = 0$ and $n_e(-L_{metal}) = n_e^0$)

n_i Number density of solute i. ($\nabla n_i(L_{sol}) = \nabla n_i(0) = 0$)

x Position in the system ($x < 0$: metal phase, $x \geq 0$: solution phase)

ϕ Electrostatic potential. ($\phi(L_{sol}) = 0$ and $\nabla\phi(-L_{metal}) = 0$)

DEPENDENT VARIABLES

C_d Differential capacitance, (Eq. 25)

C_H Helmholtz capacitance (Eq. 26)

l_D Debye length ($\left[k_B T \epsilon_0 \epsilon_{eff}^0 / (e_0^2 \sum_{i=1}^N z_i^2 n_i^0)\right]^{0.5}$)

L_{metal} Domain length of the metal phase (3.0 nm)

L_{sol} Domain length of the solution phase ($\max(20\ l_D(c_i^0), 6.0\ \text{nm})$)

n_i^0 Number density of solute *I* in the bulk. ($c_i^0 N_{avo}$)

n_e^0 Valent electron density in the bulk metal. ($3/(4\pi r_{ws}^3)$)

r_{ave} Average ion radius ($(\sum_{i=1}^N r_i)/N$)

V_i Molecular volume of solute i ($4\pi r_i^3/3$)

x_{ss} Intermediate variable for solute-solute interaction ($\left[e_0^2 r_{ave}^2 (\sum_{i=1}^N z_i^2 n_i)/\left(\epsilon_0 \epsilon_{eff}^0 k_B T\right)\right]^{0.5}$)

$\Delta\phi_{WF}$ Potential correction for work function ($\Phi_{vac}^{exp} - \Phi_{vac}^{calc}$, Table 1)

ε_{elec}^{ps} Structureless pseudopotential (Eq. 17)

ε_{elec}^{txc} Kinetic, exchange, and correlation energy of the electron (Eq. 16)

ε_{mix}^{id} Entropy from ideal mixing (Eq. 7)

ε_{mix}^{size} Entropy due to the difference in the species' molar volume (Eq. 9)

ε_{mix}^{slv} Solvent's entropy considering the finite size of solute molecules (Eq. 8)

ε_{ss}^{ion} Ion-ion interaction in $y - z$ plane (Eq. 20)

ϵ_{eff} Effective dielectric constant (Eq. S32 in SI)

ϵ_{eff}^0 Effective dielectric constant at bulk solution ($\epsilon_s^0 - \sum_{i=1}^N (n_i^0\ \beta_i / N_{avo})$)

$\epsilon_{eff}^{\nabla\phi=0}$ Effective dielectric constant without electric field ($\epsilon_s^0 - \sum_{i=1}^N (n_i\ \beta_i / N_{avo})$)

η_i Fraction of remaining space for solute $k > i$. ($1 - \sum_{k \le i} n_k V_k$)

μ_{elec} Chemical potential of the electron (Eq. 18)

$\mu_{mix,i}$ Chemical potential due to the mixing in the bulk solution (Eq. 10)

μ_{ps}^{m} Pseudopotentials in the metal (Eq. S29)

μ_{ps}^{s} Pseudopotentials in the solution. (–0.043 eV)

μ_{ss}^{ref} Reference chemical potential for the solute-solute interaction (Eq. 21)

$\mu_{ws,i}$ Chemical potential for wall-solute/solvent interactions ($\mu_{cut}\Theta(r_i - x)$)

σ_{ion} Surface charge density in the solution phase (Eq. 23)

σ_{metal} Surface charge density in the metal phase (Eq. 24)

σ_{tot} Total surface charge density ($\sigma_{ion} + \sigma_{metal}$)

Φ_{vac}^{calc} Calculated vacuum work function with $\Delta\phi_{WF} = 0$.

ω_{elec} Electron energy (Eq. 15)

ω_{els} Electrostatic energy (Eq. 11)

ω_{els}^{chg} Coulombic energy of charged species (Eq. 13)

ω_{els}^{ef} Energy from electric field (Eq. 12)

ω_{els}^{pol} Polarization energy of solvent and solute molecules (Eq. 14)

ω_{mix} Mixing entropy (Eq. 6)

ω_{ss} Solute-solute interaction (Eq. 19)

ω_{tot} Local grand potential. (Eq. 4)

ω_{ws} Wall (electrode)-solute non-electrostatic interaction (Eq. 22)

Subscript i Identifier of solute species. ($V_1 \geq \cdots \geq V_N$)

OTHER VARIABLES

D Diffusion coefficient (~10^{-9} m^2/s)

Ω_{tot} Total grand potential (Eq. 2)

V Volume of the system

N Number of the solute species

$\bar{\Omega}_{tot}$ Volumetric total grand potential (Ω_{tot}/V)

G_{ads} Adsorption free energy for ClO_4^- adsorption on Pt (111) (0.65 eV, fitted)

α_1 Relaxation parameter for ClO_4^- adsorption on Pt (111) (4.72 nm^{-1}, fitted)

r_a^{ads} Effective radius of adsorbed ClO_4^- adsorption on Pt (111) (0.40 nm, fitted)

$S_{k,j}$ Sensitivity of EDL property k on the material property j ($S_{k,j} \coloneqq m_j(\Delta e_{k,j}/\Delta m_j)$)

m_j Base value of the material property j

$\Delta e_{k,j}$ Shift of the EDL property k due to the shift in the material property j

Δm_j Shift in the material property j.

FUNCTIONS

Y_0 Bessel function of the second kind of order 0

Y_1 Bessel function of the second kind of order 1

Θ Heaviside step function ($\Theta(x > 0) = 1$ and $\Theta(x < 0) = 0$)

REFERENCES

(1) Bockris, J. O. M.; Reddy, A. K. N.; Gamboa-Aldeco, M. *Mordern Electrochemistry 2A Fundamentals of Electrodics, 2nd edition*; Klumer Academic/ Plenum Publishers, 2018, pp.871-895.

(2) Ringe, S.; Morales-Guio, C. G.; Chen, L. D.; Fields, M.; Jaramillo, T. F.; Hahn, C.; Chan, K. Double layer charging driven carbon dioxide adsorption limits the rate of electrochemical carbon dioxide reduction on Gold. *Nat Commun* **2020**, *11* (1), 33, pp.1-11. DOI: 10.1038/s41467-019-13777-z.

(3) Valette, G. Double layer on silver single crystal electrodes in contact with electrolytes having anions which are slightly specifically adsorbed Part III. the (111) face. *J. Electroanal. Chem.* **1989**, *269*, pp.191-203.

(4) Pajkossy, T.; Kolb, D. M. Double layer capacitance of Pt (111) single crystal electrodes. *Electrochimica Acta* **2001**, *46*, pp.3063-3071.

(5) Ojha, K.; Arulmozhi, N.; Aranzales, D.; Koper, M. T. M. Double Layer at the Pt(111)–Aqueous Electrolyte Interface: Potential of Zero Charge and Anomalous Gouy–Chapman Screening. *angew Chem Int Ed* **2020**, *59*, pp.711-715.

(6) Huang, J. Zooming into the Inner Helmholtz Plane of Pt(111)-Aqueous Solution Interfaces: Chemisorbed Water and Partially Charged Ions. *JACS Au* **2023**, *3* (2), pp.550-564. DOI: 10.1021/jacsau.2c00650.

(7) Schmickler, W.; Santos, E. *Interfacial Electrochemistry*; Springer-Verlag Berlin Heidelberg, 2010, pp.5-50. DOI: 10.1007/978-3-642-04937-8.

(8) Zenyuk, I. V.; Lister, S. Spatially Resolved Modeling of Electric Double Layers and SurfaceChemistry for the Hydrogen Oxidation Reaction in Water-FilledPlatinum−Carbon Electrodes. *J. Phys. Chem. C* **2012**, *116*, pp.9862-9875.

(9) Zenyuk, I. V.; Litster, S. Modeling ion conduction and electrochemical reactions in water films on thin-film metal electrodes with application to low temperature fuel cells. *Electrochimica Acta* **2014**, *146*, pp.194-206. DOI: 10.1016/j.electacta.2014.08.070.

(10) Saha, P.; Zenyuk, I. V. Electric Double Layer at the Polycrystalline Platinum−Electrolyte Interface Probed by the Electrokinetic Streaming Current Method *The Journal of Physical Chemistry C* **2021**, p.*125*, 19706-19715.

(11) Fumagalli, L.; Esfandiar, A.; Fabregas, R.; Hu, S.; Ares, P.; Janardanan, A.; Yang, Q.; Radha, B.; Taniguchi, T.; Watanabe, K.; et al. Anomalously low dielectric constant of confined water. *Science* **2018**, *360*, pp.1339-1342.

(12) Rezaei, M.; Mitterwallner, B. G.; Loche, P.; Uematsu, Y.; Netz, R. R.; Bonthuis, D. J. Interfacial, Electroviscous, and Nonlinear Dielectric Effects on Electrokinetics at Highly Charged Surfaces. *J Phys Chem B* **2021**, *125* (18), pp.4767-4778. DOI: 10.1021/acs.jpcb.0c11280

(13) Becker, M.; Loche, P.; Rezaei, M.; Wolde-Kidan, A.; Uematsu, Y.; Netz, R. R.; Bonthuis, D. J. Multiscale Modeling of Aqueous Electric Double Layers. *Chem Rev* **2024**, *124* (1), pp.1-26. DOI: 10.1021/acs.chemrev.3c00307

(14) Li, X. Y.; Jin, X. F.; Yang, X. H.; Wang, X.; Le, J. B.; Cheng, J. Molecular understanding of the Helmholtz capacitance difference between Cu(100) and graphene electrodes. *J Chem Phys* **2023**, *158* (8), 084701, pp.1-9 . DOI: 10.1063/5.0139534

(15) Limmer, D. T.; Willard, A. P.; Madden, P.; Chandler, D. Hydration of metal surfaces can be dynamically heterogeneous and hydrophobic. *Proceedings of the National Academy of Sciences* **2013**, *110* (11), pp.4200-4205. DOI: 10.1073/pnas.1301596110.

(16) Booth, F. The Dielectric Constant of Water and the Saturation Effect. *The Journal of Chemical Physics* **1951**, *19* (4), pp.391-394. DOI: 10.1063/1.1748233.

(17) Dhattarwal, H. S.; Gao, A.; Remsing, R. C. Dielectric Saturation in Water from a Long-Range Machine Learning Model. *J Phys Chem B* **2023**, *127* (16), pp.3663-3671. DOI: 10.1021/acs.jpcb.3c00390.

(18) Gongadze, E.; Iglic, A. Decrease of permittivity of an electrolyte solution near a charged surface due to saturation and excluded volume effects. *Bioelectrochemistry* **2012**, *87*, pp.199-203. DOI: 10.1016/j.bioelechem.2011.12.001

(19) Bikerman, J. J. XXXIX. Structure and capacity of electrical double layer. *The London, Edinburgh, and Dublin Philosophical Magazine and Journal of Science* **2009**, *33* (220), pp.384-397. DOI: 10.1080/14786444208520813.

(20) Huang, J. Density-Potential Functional Theory of Electrochemical Double Layers: Calibration on the Ag(111)-KPF(6) System and Parametric Analysis. *J Chem Theory Comput* **2023**, *19* (3), pp.1003-1013. DOI: 10.1021/acs.jctc.2c00799.

(21) Johnson, E.; Haussener, S. Contrasting Views of the Electric Double Layer in Electrochemical CO2 Reduction: Continuum Models vs Molecular Dynamics. *The Journal of Physical Chemistry C* **2024**, *in press*. DOI: 10.1021/acs.jpcc.4c03469.

(22) *A Primer in Density Functional Theory*; Springer, 2003, pp.1-122. DOI: 10.1007/BFb0106736.

(23) Luque, N. B.; Woelki, S.; Henderson, D.; Schmickler, W. A model for the electrical double layer combining integral equation techniques with quantum density functional theory. *Electrochimica Acta* **2011**, *56* (21), pp.7298-7302. DOI: 10.1016/j.electacta.2011.06.049.

(24) Skulason, E.; Karlberg, G. S.; Rossmeisl, J.; Bligaard, T.; Greeley, J.; Jonsson, H.; Norskov, J. K. Density functional theory calculations for the hydrogen evolution reaction in an electrochemical double layer on the Pt(111) electrode. *Phys Chem Chem Phys* **2007**, *9* (25), pp.3241-3250. DOI: 10.1039/b700099e

(25) Le, J.-B.; Fan, Q.-Y.; Li, J.-Q.; Cheng, J. Molecular origin of negative component of Helmholtz capacitance at electrified Pt(111)/water interface. *Science Advances* **2020**, *6*, eabb1219, pp.1-7.

(26) Shin, S. J.; Kim, D. H.; Bae, G.; Ringe, S.; Choi, H.; Lim, H. K.; Choi, C. H.; Kim, H. On the importance of the electric double layer structure in aqueous electrocatalysis. *Nat Commun* **2022**, *13* (1), p.174. DOI: 10.1038/s41467-021-27909-x.

(27) Jinnouchi, R.; Anderson, A. B. Electronic structure calculations of liquid-solid interfaces: Combination of density functional theory and modified Poisson-Boltzmann theory. *Physical Review B* **2008**, *77* (24), 245417, pp.1-18. DOI: 10.1103/PhysRevB.77.245417.

(28) Letchworth-Weaver, K.; Arias, T. A. Joint density functional theory of the electrode-electrolyte interface: Application to fixed electrode potentials, interfacial capacitances, and potentials of zero charge. *Physical Review B* **2012**, *86* (7), 075140, pp.1-16. DOI: 10.1103/PhysRevB.86.075140.

(29) Smith, J. R. Self-Consistent Many-Electron Theory of Electron Work Functions and Surface Potential Characteristics for Selected Metals. *Physical Review* **1969**, *181* (2), pp.522-529. DOI: 10.1103/PhysRev.181.522.

(30) Ashcroft, N. W. Electron-ion pseudopotentials in metals. *Physics letters* **1966**, *23* (1), pp.48-50.

(31) Moriarty, J. A. Density-functional formulation of the generalized pseudopotential theory. III. Transition-metal interatomic potentials. *Phys Rev B Condens Matter* **1988**, *38* (5), pp.3199-3231. DOI: 10.1103/physrevb.38.3199.

(32) Perdew, J. P.; Tran, H. Q.; Smith, E. D. Stabilized jellium: Structureless pseudopotential model for the cohesive and surface properties of metals. *Phys Rev B Condens Matter* **1990**, *42* (18), pp.11627-11636. DOI: 10.1103/physrevb.42.11627.

(33) Wills, J. M.; Harrison, W. A. Interionic interactions in transition metals. *Physical Review B* **1983**, *28* (8), pp.4363-4373. DOI: 10.1103/PhysRevB.28.4363.

(34) Henderson, D.; Leiva, E.; Schmickler, W. The jellium/hard sphere electrolyte interface. *Berichte der Bunsengesellschaft für physikalische Chemie* **1987**, *91* (4), pp.280-284. DOI: 10.1002/bbpc.19870910408.

(35) Huang, J.; Li, P.; Chen, S. Potential of zero charge and surface charging relation of metal-solution interphases from a constant-potential jellium-Poisson-Boltzmann model. *Physical Review B* **2020**, *101* (12), 125422, pp.1-9. DOI: 10.1103/PhysRevB.101.125422.

(36) Schmickler, W.; Henderson, D. The interphase between jellium and a hard sphere electrolyte. A model for the electric double layer. *The Journal of Chemical Physics* **1984**, *80* (7), pp.3381-3386. DOI: 10.1063/1.447092.

(37) Wu, J. Understanding the Electric Double-Layer Structure, Capacitance, and Charging Dynamics. *Chem Rev* **2022**, *122* (12), pp.10821-10859. DOI: 10.1021/acs.chemrev.2c00097.

(38) Zhang, Z.; Gao, Y.; Chen, S.; Huang, J. Understanding Dynamics of Electrochemical Double Layers via a Modified Concentrated Solution Theory. *Journal of The Electrochemical Society* **2019**, *167* (1), 013519, pp.1-9. DOI: 10.1149/2.0192001jes.

(39) Wu, J. *Variational Methods in Molecular Modeling*; Springer, 2017, pp.19-24. DOI: 10.1007/978-981-10-2502-0.

(40) Borukhov, I.; Andelman, D. Steric Effects in Electrolytes: A Modified Poisson-Boltzmann Equation. *Physical Review Letters* **1997**, *79* (3), pp.435-438.

(41) Borukhov, I.; Andelman, D.; Orland, H. Adsorption of large ions from an electrolyte solution: a modified Poisson-Boltzmann equation. *Electrochimica Acta* **2000**, *46*, pp.221-229.

(42) Kornyshev, A. A. Double-Layer in Ionic Liquids: Paradigm Change? *J. Phys. Chem. B* **2007**, *111*, pp.5545-5557.

(43) Gongadze, E.; Iglič, A. Asymmetric size of ions and orientational ordering of water dipoles in electric double layer model - an analytical mean-field approach. *Electrochimica Acta* **2015**, *178*, pp.541-545. DOI: 10.1016/j.electacta.2015.07.179.

(44) Maggs, A. C.; Podgornik, R. General theory of asymmetric steric interactions in electrostatic double layers. *Soft Matter* **2016**, *12* (4), pp.1219-1229. DOI: 10.1039/c5sm01757b

(45) Harris, F. E.; O'Konski, C. T. Dielectric properties of aqueous ionic solutions at microwave frequencies. *The journal of physical chemistry* **1956**, *61*, pp.310-319.

(46) Gavryushov, S.; Linse, P. Polarization Deficiency and Excess Free Energy of Ion Hydration in Electric Fields. *J. Phys. Chem. B* **2003**, *107*, pp.7135-7142.

(47) Russier, V. V.; Badiali, J. P. Calculation of the electronic work function of Cu and Ag from an extended jellium model. *Phys Rev B Condens Matter* **1989**, *39* (18), pp.13193-13200. DOI: 10.1103/physrevb.39.13193.

(48) Valette, G. Double layer on silver single crystal electrodes in contact with electrolytes having anions which are slightly specifically adsorbed Part I. the (110) face. *J. Electroanal. Chem.* **1981**, *122*, pp.285-297.

(49) Ruban, A.; Hammer, B.; Stoltze, P.; Skriver, H. L.; Nørskov, J. K. Surface electronic structure and reactivity of transition and noble metals. *Journal of Molecular Catalysis A: Chemical* **1997**, *115*, pp.421-429.

(50) Hasegawa, M.; Young, W. H. Bulk moduli of solid and liquid metals. *J. Phys. F: Metal Phys* **1981**, *11*, pp.977-994.

(51) Chelvayohan, M.; Mee, C. H. B. Work function measurements on (110), (100) and (111) surfaces of silver. *J. Phys. C: Solid State Phys.* **1982**, *15*, pp.2305-2312.

(52) Boronat-González, A.; Herrero, E.; Feliu, J. M. Determination of the potential of zero charge of Pt/CO electrodes using an impinging jet system. *Journal of Solid State Electrochemistry* **2020**, *24* (11-12), pp.2871-2881. DOI: 10.1007/s10008-020-04654-7.

(53) Lide, D., R. *CRC Handbook of Chemistry and Physics*; CRC Press, 2005, 12-p.124.

(54) Marcus, Y. Ionic Radii in Aqueous Solutions. *Chem Rev* **1988**, *88*, pp.1475-1498. DOI: 10.1021/cr00090a003,.

(55) Glueckauf, E. Bulk Dielectric Constant of Aqueous Electrolyte Solutions. *Trans. Faraday Soc.* **1964**, *60*, pp.1637-1645.

(56) Trasatti, S. THE ABSOLUTE ELECTRODE POTENTIAL: AN EXPLANATORY NOTE. *Pure & AppL Chem.* **1986**, *58* (7), pp.955-966.

(57) Grahame, D. C. Differential Capacity of Mercury in Aqueous Sodium Fluoride Solutions. I. Effect of Concentration at 25°. *J. Am. Chem. Soc.* **1954**, *76* (19), pp.4819-4823.

(58) Grahame, D. C. Capacity of the Electrical Double Layer between Mercury and Aqueous Sodium Fluoride. II. Effect of Temperature and Concentration. *J. Am. Chem. Soc.* **1957**, *79* (9), pp.2093-2098.

(59) Omura, J.; Yano, H.; Watanabe, M.; Uchida, H. Electrochemical quartz crystal microbalance analysis of the oxygen reduction reaction on Pt-based electrodes. Part 1: Effect of adsorbed anions on the oxygen reduction activities of Pt in HF, HClO4, and H2SO4 solutions. *Langmuir* **2011**, *27* (10), pp.6464-6470. DOI: 10.1021/la200694a.

(60) Omura, J.; Yano, H.; Tryk, D. A.; Watanabe, M.; Uchida, H. Electrochemical quartz crystal microbalance analysis of the oxygen reduction reaction on Pt-based electrodes. Part 2: adsorption of oxygen species and ClO4(-) anions on Pt and Pt-Co alloy in HClO4 solutions. *Langmuir* **2014**, *30* (1), pp.432-439. DOI: 10.1021/la404188p.

(61) Mathew, K.; Sundararaman, R.; Letchworth-Weaver, K.; Arias, T. A.; Hennig, R. G. Implicit solvation model for density-functional study of nanocrystal surfaces and reaction pathways. *J Chem Phys* **2014**, *140* (8), 084106, pp.1-8. DOI: 10.1063/1.4865107

(62) Mathew, K.; Kolluru, V. S. C.; Mula, S.; Steinmann, S. N.; Hennig, R. G. Implicit self-consistent electrolyte model in plane-wave density-functional theory. *J Chem Phys* **2019**, *151* (23), 234101, pp.1-8. DOI: 10.1063/1.5132354

(63) Islam, S. M. R.; Khezeli, F.; Ringe, S.; Plaisance, C. An implicit electrolyte model for plane wave density functional theory exhibiting nonlinear response and a nonlocal cavity definition. *J Chem Phys* **2023**, *159* (23), 234117, pp.1-24. DOI: 10.1063/5.0176308

(64) Sundararaman, R.; Letchworth-Weaver, K.; Schwarz, K. A.; Gunceler, D.; Ozhabes, Y.; Arias, T. A. JDFTx: software for joint density-functional theory. *SoftwareX* **2017**, *6*, pp.278-284. DOI: 10.1016/j.softx.2017.10.006

TABLE OF CONTENTS/ASBSTRACT GRAPHICS

For Table of Contents Only